electrochem

MDPI

Article

Impact of PAA Binder Modification on the Structure and Chemistry of the SEI on Si in Li-Ion Batteries

Belinda Awudu Agamah [1], Md Wahiduzzaman [2], Santosh Kiran Balijepalli [3], Morgan Stefik [2] and William E. Mustain [1,*]

[1] Department of Chemical Engineering, University of South Carolina, Columbia, SC 29208, USA; bagamah@email.sc.edu
[2] Department of Chemistry and Biochemistry, University of South Carolina, Columbia, SC 29208, USA; wahiduzm@email.sc.edu (M.W.); stefik@mailbox.sc.edu (M.S.)
[3] Office of the Vice President for Research, University of South Carolina, Columbia, SC 29208, USA; skiran@sc.edu
* Correspondence: mustainw@mailbox.sc.edu

Abstract

Silicon is a promising replacement for graphite anodes in lithium-ion batteries for electric vehicles due to its exceptionally high theoretical capacity. However, large volume expansion during cycling and unstable solid electrolyte interphase (SEI) formation have hindered its practical implementation. Extensive efforts have focused on mitigating these challenges, including binder engineering. An effective binder for silicon anodes must provide strong mechanical integrity, enable formation of a robust SEI, and be compatible with solvent-based processing. Polyacrylic acid (PAA) is widely used for silicon anodes, but PAA-based slurries exhibit significant phase separation, limiting industrial processability and compromising structural and SEI stability. Here, we compare PAA with in-house synthesized poly(methacrylic acid) (PMAA), which has an additional methyl group. Electrodes fabricated with PMAA exhibit higher coulombic efficiency and form a more stable SEI than those using PAA. Although the SEI species for Si anodes with a PMAA binder are chemically similar to those with PAA, the SEI gradually thickens with the PMAA binder, whereas electrodes made with PAA show significant fresh SEI production. This has a positive impact on the electrochemical performance and the overall coulombic efficiency.

Keywords: lithium-ion battery; silicon; anode; solid electrolyte interphase; binder

1. Introduction

Since the inception of fossil fuel-powered locomotion, the transportation sector has been a major source of air pollution and greenhouse gas emissions [1,2]. This has necessitated research into more sustainable alternatives to conventional combustion engine-based transportation systems. Vehicle electrification has gained significant attention as a scalable and environmentally friendly alternative to reduce our dependence on fossil fuels. The International Energy Agency has set a target to make 30% of all new vehicles electric vehicles (EVs) by 2030 [3]. This is, however, contingent upon the continued development of advanced EV battery technologies that improve energy density, cycle life, safety, and cost.

Over the past three decades, significant advancements in Li-ion battery technologies have made them the most efficient and reliable energy storage technology for EVs due to their high energy density, long cycle life, no memory effect, broad operating temperature range, low self-discharge rate, and ability to support fast charging [4,5]. These attributes also

Check for updates

Received: 12 October 2026
Revised: 6 November 2026
Accepted: 17 November 2026
Published: 21 November 2026

Copyright: © 2026 by the authors. Licensee MDPI, Basel, Switzerland. This article is an open access article distributed under the terms and conditions of the Creative Commons Attribution (CC BY) license.

explain why lithium-ion batteries dominate consumer electronics such as mobile phones, digital cameras laptops, power tools and portable devices.

Conventional lithium-ion batteries employ an intercalation-type graphite anode with a gravimetric and volumetric capacity of 372 mAh/g and 735 mAh/cm^3, respectively, which limits their overall energy density and effectiveness for future EV applications [6]. Because the weight and volume of the battery generally cannot be increased, increasing the specific capacity of the electrode materials appears to be the most promising way to increase the amount of stored energy. To compete with gasoline-powered cars, next-generation lithium-ion battery chemistries [7–9] have been studied with the aim of achieving higher energy densities to enable longer driving range.

Silicon is widely considered to be the most promising alternative anode material due to its high theoretical capacity (4200 mAh/g at full lithiation), which far exceeds that of conventional graphite. However, the anisotropic expansion and contraction of silicon anodes during charge/discharge present a variety of limitations, including the following: (a) continuous disintegration of the solid electrolyte interphase (SEI) layer on the silicon anode, leading to an increase in SEI layer thickness and electrolyte consumption; and (b) loss of electrical contact between the active material, binder, and current collector [10–12]. These limitations typically result in significant degradation in electrochemical performance over time, such as reduced cyclability and lower operating voltage. Thus, improvements in electrical contact and SEI stability are necessary for the practical utilization of silicon.

In the past several years, significant advancements have been made to mitigate the rapid capacity decay in silicon anodes by either optimizing electrode-level or non-electrode parameters. Non-electrode-level strategies such as pre-lithiation [13] and electrolyte optimization [14,15] have been shown to improve the cycling performance by forming an earlier SEI passivating layer that inhibits further decomposition of the electrolyte. Electrode-level strategies including silicon structure design [16,17], composites with graphite [7], and SiO_2 surface coating have been studied [18]. Binder engineering is also recognized as an effective way to improve the electrochemical performance of silicon-based anodes [7,19]. Because binders constitute only a small fraction of the electrode mass and do not directly contribute to the overall achieved capacity of the anode material, they have historically received less attention [20]. Binders play a critical role in maintaining electronic conductivity via adhesion of electrode materials to carbon additives and the current collector while also playing a role in ionic conductivity, thereby reducing polarization and improving the overall rate performance of the anode [20,21].

The primary consideration in choosing a suitable binder candidate is its ability to maintain the adhesion between the active material, conducting material, and the current collector, as well as the electrode as a whole, during cycling. However, for silicon anodes, additional criteria must be considered: (1) A strong interaction between the surface of the silicon particle and binder. Binders like poly(acrylic acid) (PAA), carboxymethyl cellulose (CMC), and sodium alginate (SA) have carboxylic and hydroxyl functional groups. Thus, they have the natural ability to form hydrogen bonds with SiO_2 and the hydroxyl groups on the native surface of the silicon particles. Binders that barely adhere to silicon through weak Van der Waals forces, like polyvinylidene fluoride (PVDF) and polytetrafluoroethylene (PTFE), are unsuitable for silicon anodes [22]; (2) Formation of a robust and stable SEI layer. A recent study by Eshetu et al. [23] revealed that the binder also participates in the formation of the SEI layer. Thus, a binder for silicon anodes should be able to help form a stable interface with the silicon to prevent continuous electrolyte reduction; (3) Good electrical conductivity. Silicon in its natural form is a semiconductor. Additionally, it undergoes significant volume expansion that leads to pulverization. It is therefore imperative to have conductive paths to the active material, where the binder must maintain physical connections between the

active material, conductive additives, and the current collector after pulverization; and (4) Processability. To form uniform slurries, the binder should have the ability to form a stable and homogeneous slurry dispersion with silicon and the conducting material in a solvent without noticeable agglomeration or phase separation [24].

Amongst the wide array of binders used in silicon anodes, PAA binders are the most widely used and studied. Various researchers have studied the role of the binder, from its mechanical properties to its effect on the electrochemical performance of silicon-based anodes. Notably, Parikh et al. [25] studied the role that the PAA binder plays in the formation of SEI. They discovered that PAA directly helped to form passivating sulfide species (from LiTFSI) around the individual silicon particles, enhancing capacity retention. They also showed that the PAA binder has better cycling performance than carboxymethyl cellulose (CMC) binder. Other researchers have focused on increasing the mechanical integrity by crosslinking PAA, with the aim of avoiding chain slipping during cycling. Chen et al. [26] compared the performance of a linear PAA binder with PAA crosslinked with Tannic acid and showed that the crosslinked binder achieved an impressive 84% capacity retention after 450 cycles. One of the main reasons why PAA is used is due to its numerous carboxylic groups, which enhance adhesion between the silicon particles, the conducting material, and the current collector. Additionally, these carboxylic groups form hydrogen bonds with the surface of the silicon [27]. However, the presence of interchain hydrogen bonds between these carboxylic groups leads to the formation of a randomly coiled structure, which reduces the number of sites available for bonding with the silicon particle. This leads to polymer segregation, ultimately leading to relatively poor electrode adhesion [28]. To prevent interchain hydrogen bonding, many researchers have come up with strategies such as prelithiation of the binder with a Li precursor to transform the chains into stretched conformations [29,30]. Hu et al. [31] studied the effect of prelithiation of PAA with LiOH on the cycling performance and slurry stability for Si/G composite electrodes. The method increased slurry viscosity at low sheer rates, which reduced particle sedimentation and enhanced slurry stability. However, the introduction of LiOH resulted in substantial degradation in the achieved capacity. It was reported that at 50 mol% LiOH/COOH, electrodes achieved approximately 51% capacity retention after 100 cycles, which is 15% lower than the capacity retention of cells made with pure PAA. These findings demonstrate the need to find alternative approaches to stabilize slurries without compromising cell performance.

In this manuscript, the electrochemical properties of silicon anodes with a poly(methacrylic acid) (PMAA) binder are investigated and compared to conventional PAA. Here, PMAA is a derivative of PAA with an additional methyl group attached to each mer unit along the backbone. SEM is used to visualize the morphological changes that occur on the surface of the electrode after 1 and 10 electrochemical cycles. Since the type of binder also affects the nature of the SEI layer around the Si, TEM and XPS are used to determine the changes in structure and chemical composition of the SEI induced after repeated cycling.

2. Materials and Methods

2.1. Materials

Silicon nanopowder (lot number: 0141-010324) with an average particle size between 30 and 50 nm and 98% purity was purchased from Nanostructured and Amorphous Materials, Inc., Los Alamos, NM, USA. Poly(acrylic acid)—the powder (product number: 03312-100; MW 450,000) and 30% solution (product number: 30,000; MW 30,000)—was purchased from Polysciences., Warrington, PA, USA. Super P was purchased from MSE supplies., Tuscon, AZ, USA and was used as the conductive carbon in silicon anodes. 99.9% purity lithium hexafluorophosphate ($LiPF_6$) was purchased from Sigma Aldrich., St. Louis, MO, USA. Ethylene carbonate (2053993CT) and diethyl carbonate (A0382282) at 99+% purity

were purchased from Acros Organics., Waltharm, MA, USA. Methacrylic acid monomer (BeanTown Chemical, ≥99%, Hudson, NH, USA) was passed through a basic alumina column to remove the inhibitor prior to use. Ethanol (200 proof, Fisher, Waltham, MA, USA) was dried at room temperature over 50% *w*/*w* of molecular sieves (3 Å, 8–12 mesh, Acros Organics, Geel, Belgium). 2,2′-Azobis(2-methylpropnitrile) (AIBN, 98%, Sigma-Aldrich, Burlington, MA, USA) was recrystallized from methanol and stored in a freezer (−20 °C). 2-Cyano-2-propyl benzodithioate (CPDB) (>97%, Millipore Sigma, Milwaukee, WI, USA) was used as received.

2.2. Synthesis of Poly(methacrylic Acid) (PMAA)

CPDB (80 mg, 0.36 mmol, 1 equiv.), methacrylic acid (14 g, 162 mmol, 450 equiv.), and AIBN (5.9 mg, 0.036 mmol, 0.1 equiv.) were mixed in 20 mL of ethanol in a Schlenk flask. The mixture underwent three cycles of freeze–pump–thaw to remove the dissolved gases and was subsequently brought into an argon-filled glovebox to backfill with inert gas. The polymerization was then carried out in a preheated oil bath at 60 °C for 16 h. Once the polymerization was complete, the reaction was cooled in a freezer for ten minutes before venting. An aliquot of crude product was collected for conversion analysis, showing a 90% conversion, and was verified by ^{1}H-NMR end-group analysis, resulting in a final molecular weight of 35 kg mol^{-1} (Figure S1). The product was purified by washing three times with a tenfold excess of diethyl ether to remove unreacted monomer. A pink solid was obtained after drying under vacuum.

2.3. Polymer Characterization

^{1}H-NMR spectra were collected using a Bruker Avance III-HD 400 with deuterated methanol as the solvent. Gel Permeation Chromatography (GPC) analysis (Figure S1) was conducted using a refractive index detector with DMF, with 10 mM LiBr as the mobile phase at a flow rate of 1.0 mL min^{-1} and a temperature of 80 °C. The GPC was composed of a Waters 515 HPLC pump, a Waters 2410 refractive index detector, and three Styragel columns (HR2, HR4, and HR5) in the effective molecular weight range of 0.5–20, 5–600, and 50–4000 kg mol^{-1}, respectively. The data was analyzed using custom MATLAB scripts (version R2022b, The MathWorks, Inc., Natick, MA, USA). A series of twelve monodisperse polyethylene glycol standards with molecular weights ranging from 200 to 5,011,872 g mol^{-1} were used for GPC calibration.

2.4. Silicon Anode Fabrication and Coin Cell Assembly

Anode slurry was made with silicon nanopowder, binder (PAA or PMAA), and Super P in a 60:35:5 ratio. The desired amount of binder powder was first dissolved in DI water (6 wt% for PAA and 5 wt% for PMAA) to prepare the binder solution. In a typical setup, 583 mg of 6 wt% PAA or 700 mg of 5 wt% PMAA (corresponding to 35 mg of binder) was added to a vial. Then, 60 mg of silicon nanopowder and 5 mg of Super P were dry-mixed in a mortar and pestle and then transferred into the vial containing the binder solution. Next, 700 µL of solvent (DI water) was pipetted into the vial containing 100 mg of total solids to obtain a slurry with moderate viscosity. The slurry was then subjected to 3 cycles of 45 min sonication and 5 min of stirring, after which the sample was stirred overnight. The as-prepared slurry was spray-coated onto a 72 µm thick copper foil current collector with an Iwata-Medea Eclipse HP-CS spray gun. The electrode was left to air-dry for 4 h and then dried at 80 °C for 8 h under vacuum. The electrodes were punched into 14 mm disks. The punched electrodes were transferred to an Argon-filled (ultra-high purity 5.0 argon, Airgas, Radnor, PA, USA) MBraun Labmaster SP glovebox (O_2 and H_2O < 0.1 ppm) for coin cell assembly. The electrode loading was between 0.3 and 0.5 mg/cm^2 for all electrodes.

Several half cells with each anode were made using CR2032 coin cells where 15 mm diameter lithium foil was used as the counter and reference electrode. First, the lithium foil was polished and positioned at the center of the coin cell base. Second, 15 µL of 1M lithium hexafluorophosphate ($LiPF_6$) in 1:1 *v/v* ethylene carbonate/diethyl carbonate (EC/DEC) was added on top of the lithium foil. A 2325 tri-layer PP/PE/PP Celgard separator with a 19 mm diameter was centered on top of the lithium/electrolyte surface. An additional 15 µL of electrolyte was added on top of the separator. A 19.5 mm gasket was placed along the outer diameter of the separator inside the coin cell base to prevent short-circuiting, facilitate proper centering of the working electrode, and enable proper sealing of the cell. The 14 mm diameter working electrode was then placed such that the side with the active material faced the separator/electrolyte surface. A 15.5 mm spacer disk and spring were then placed to keep components in place and ensure uniform distribution of pressure in the cell. Finally, the coin cell cap was placed, and an MTI hydraulic press (MSK-110) was used to seal the cell at a pressure of 750 PSI.

2.5. Electrochemical Measurements

Galvanostatic charge/discharge of the coin cells was done at room temperature from 0.005 to 1.5 V vs. Li/Li^+ at a C/10 rate using a Neware CT-4008Tn-5V10mA-HWX-U Battery cycler (Neware Technology, Shenzhen, China). The current was calculated based on a theoretical capacity of 3600 mAh/g for silicon. The Galvanostatic charge/discharge data allowed the cycle life performance of the anode material, coulombic efficiency, and the voltage response of the cell to be evaluated. Electrochemical Impedance Spectroscopy (EIS) was conducted at room temperature over a frequency range of 0.1 Hz to 1 MHz with an amplitude of 5 mV relative to the open-circuit voltage (discharged/delithiated to the cutoff voltage) using a Metrohm Autolab PGSTAT204 potentiostat (Metrohm., Riverview, FL, USA). Cycled cells were typically allowed to rest at least overnight before making the EIS measurement. For all experiments, although several cells were made, data from a single representative cell is shown.

2.6. Physical and Chemical Characterization

Coin cells were disassembled and Si electrodes extracted in a glovebox after 1 and 10 cycles. The electrodes were then soaked in a DEC for 30 min to remove residual electrolyte salt on the surface of the electrode and then dried in the glovebox. The changes in the morphology of the silicon anodes induced by repeated cycling were characterized using a thermal field-emission scanning electron microscope Ziess Gemini500, FESEM (Carl Zeiss Microscopy GmbH., Jena, Germany) (equipped with an energy-dispersive X-ray spectrometer (EDS). The changes in the structure of the SEI layer were characterized using a 120kV Hitachi HT7800 transmission electron microscope (TEM) (Hitachi High-Tech Corporation, Ibaraki, Japan).

The surface chemistry of the silicon anodes before cycling, after 1 cycle, and after 10 cycles was investigated with an AXIS Ultra DLD XPS instrument (Kratos Analytical Ltd., Manchester, UK). The XPS system is equipped with a non-monochromic Al Kα source (1486.8 eV) operated at 120 W X-ray gun power, a hemispherical analyzer, a charge neutralizer, and a load lock chamber for rapid introduction of samples without breaking vacuum. The X-rays were incident at an angle of 45° with respect to the surface normal. Analysis was performed at a pressure of ~1×10^{-9} Torr, and high-resolution core-level spectra were acquired in the constant analyzer energy mode using a pass energy of 40 eV and 0.08 eV step size. The XPS experiments were performed using a low electron beam directed at the sample for charge neutralization. The binding energies (BEs) of all peaks were corrected in reference to the C 1s peak at 285 eV with an accuracy of ±−0.2 eV. The curve-fitting

procedure was carried out using the Casa XPS Version 2.3.27 software, and the peak approximation was carried out by a combination of Gaussian–Lorentzian functions, with subtraction of the Shirley-type background [32].

2.7. Characterization of Degree of Slurry Phase Separation

175 mg of binder was dissolved in DI water and added to a vial. Then, 300 mg of Si and 25 mg of Super P were dry-mixed together with a mortar and pestle and added to the vial. Next, 5 mL DI water was added to the vial, and the vial was allowed to stir overnight. After stirring, the slurry was kept in a 15 mL test tube for 7 days at room temperature. The degree of phase separation was evaluated by observing the extent of separation into layers, where clearly separated layers indicated a higher degree of phase separation. Quantitatively, the degree of phase separation was evaluated using Equation 1 below.

$$H_s = \frac{H_t}{H_i}$$

where H_s is the sedimentation ratio, H_t is the height at time t, and H_i is the initial height.

3. Results and Discussion

3.1. Electrochemical Performance

The chemical structures of PAA and PMAA are shown in Figure 1a,b, respectively. The PMAA was synthesized with a molecular weight of 35,000 g/mol using reversible addition−fragmentation chain-transfer polymerization (RAFT, Figure S1). The PAA binder was a commercial binder with a molecular weight of 450,000 g/mol. However, in Figure S2, a PAA binder cast film shows a uniform and smooth film, whilst a PMAA binder cast film was less uniform, with some visible cracking of the dried film. This is consistent with the PMAA binder being more rigid than the PAA binder, which is also consistent with PMAA's increased steric hinderance along the polymer backbone and its higher glass transition temperature. Here, the 80 °C slurry drying temperature is proximal to the PAA T_g, ~100 °C, enabling some softening; however, this is far below the PMAA T_g, ~200 °C, where polymer reorganization is not anticipated [33].

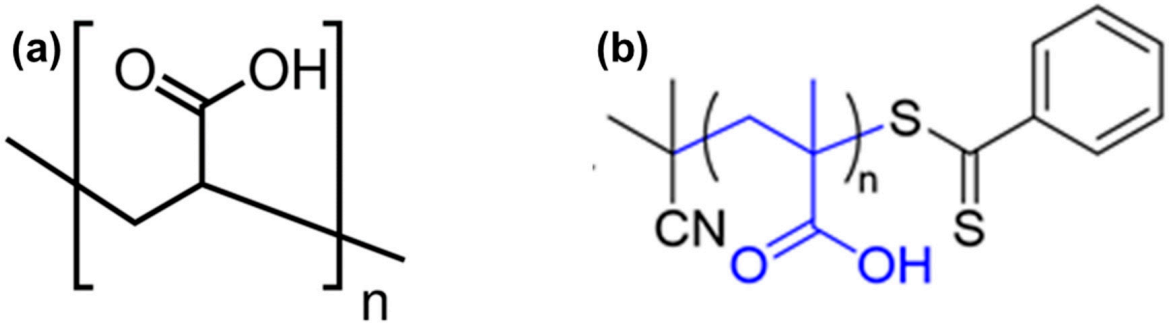

Figure 1. Structure of (**a**) PAA and (**b**) PMAA.

To evaluate the effectiveness of PMAA as a binder for silicon-based anodes, half cells with both PMAA and PAA binders were subjected to galvanostatic charge/discharge tests and EIS experiments. As shown in Figure 2a, the initial lithiation capacity for a representative PAA anode was 2117 mAh/g, and the subsequent delithiation capacity was 1626 mAh/g, resulting in a first-cycle efficiency of 77%. The coulombic efficiency increased from 77% to 88% on the second cycle and rose throughout the cycle life, but showed instability, indicating that there were likely ongoing side reactions leading to continuous consumption of electrolyte. Additionally, cells with PAA showed a capacity retention of 57% after 50 cycles

and 21% over 100 cycles. This poor cyclability is consistent with previous studies that used a PAA binder [34].

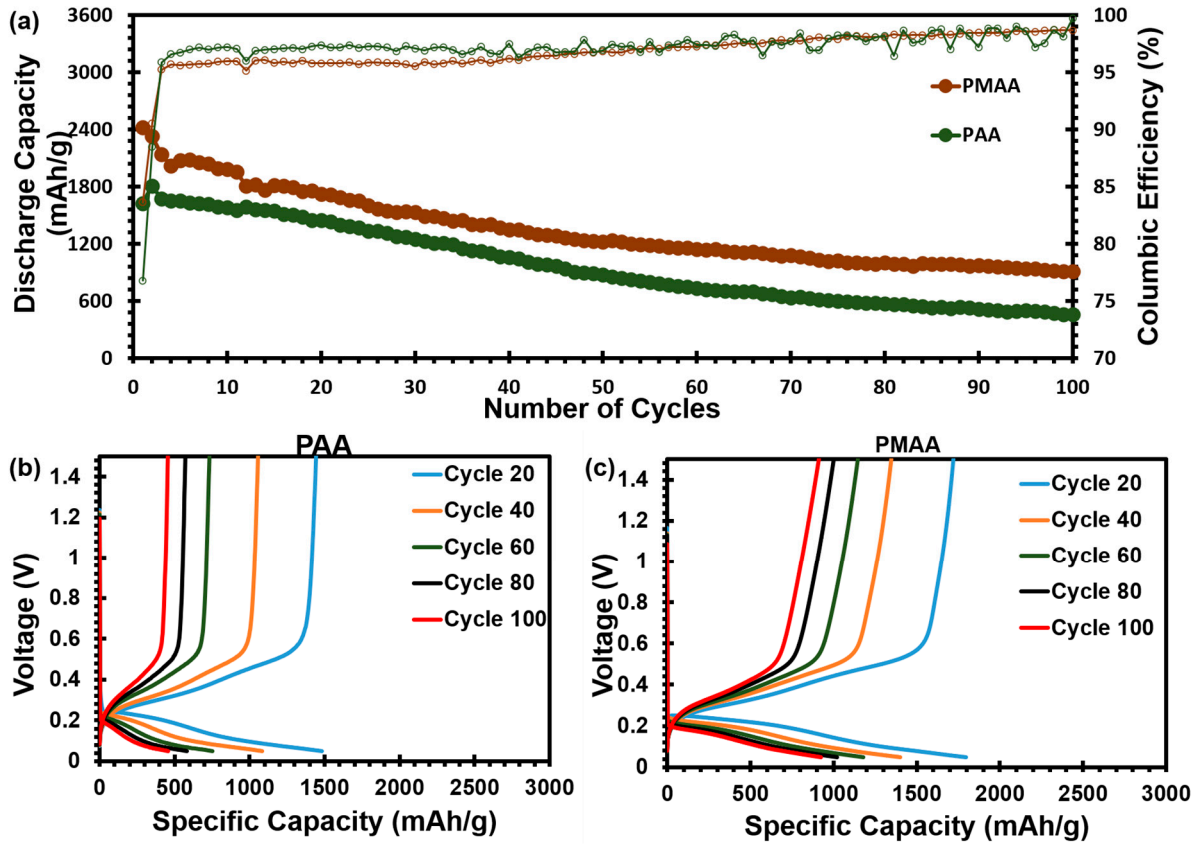

Figure 2. (**a**) Electrochemical performance (dark, large, closed markers) and coulombic efficiency (lighter, small, open markers) of silicon anode with different binders. Voltage profiles for (**b**) Si-PAA and (**c**) Si-PMAA.

Cells with PMAA, on the other hand, exhibited a much higher initial lithiation capacity of 2897 mAh/g and a delithiation capacity of 2423 mAh/g, corresponding to a first-cycle coulombic efficiency of 84%, which is 8% higher than that of PAA. The coulombic efficiency rose from 84% to 90% on the second cycle and maintained a steady linear increase as the cycle number increased—with a peak efficiency of 98.9%. The more stable coulombic efficiency observed in half cells with PMAA and the higher final coulombic efficiency indicate fewer side reactions and account for the improved cycling performance observed in the half cells with PMAA binder—where 59% of the capacity was retained over the first 50 cycles and 43% over 100 cycles.

The voltage profiles for electrodes with PAA showed discharge capacities of 1445, 1057, 731, 572, and 454 mAh/g at 20, 40, 60, 80, and 100 cycles, respectively (Figure 2b). Electrodes with a PMAA binder showed much higher discharge capacities of 1720, 1346, 1145, 1003, and 910 mAh/g at 20, 40, 60, 80, and 100 cycles, respectively (Figure 2c). Additionally, the voltage profile of cells with PAA had a very steep delithiation profile, where only 269 mAh/g is accounted for between 0.5 V and 1.5 V at cycle 20. Compared to the PAA binder, the electrodes with PMAA had a less steep delithiation voltage profile, accumulating 435 mhA/g capacity within 0.5 V and 1.5 V at cycle 20. This large increase in electrode potential from a relatively small amount of Li^+ extraction indicates the presence of larger polarization in PAA cells compared to PMAA cells. To further confirm this, the voltage profile at cycle 60 for both cells is shown in Figure S3. It can be seen that the cell with PAA

has a larger separation between the lithiation and delithiation profiles. Such polarization is consistent with less uniform mixing of conductive additives with the Si and PAA. It is worth noting that the two polymers have different molecular weights (PAA Mw 450,000 g/mol, PMAA 35,000 g/mol). To ascertain that the low cycling performance of the electrodes with PAA is not due to the larger-molecular-weight PAA binder used, electrodes were made with a PAA binder with a lower molecular weight (Mw 30,000 g/mol) comparable to that of the PMAA binder. Electrodes and cells were made, and representative performance is shown in Figure S3b. These results show that even at similar molecular weights, electrodes with a PMAA binder enable better utilization of the silicon which translates into higher accessible capacity in the initial cycles. The cycling performance of electrodes at higher loading are present in Figure S5.

Next, rate capability and EIS experiments were done with cells using both binders. The rate capability was tested over a wide range of current densities (C/25, C/10, C/5, C/2, 1C), and the results are shown in Figure 3a. Cells with PMAA binders exhibited relatively better rate performance in terms of achieved capacity and better stability than those with PAA at all rates. At low rates, i.e., C/25, C/10, C/5, and C/2, electrodes with PMAA binders showed a steady and stable electrochemical performance. Electrodes with PAA, on the other hand, showed a relatively lower achieved capacity and an unstable performance characterized by a steep decay in capacity as the cycle number increased. As the current density increased to 1C, both cell types experienced a steep decay in performance, suggesting that both electrodes experienced relatively high polarization at high rates. When the current density was reduced to lower rates, both electrodes could fully recover a substantial fraction of their initial achieved capacity, with PMAA electrodes still showing higher overall achieved capacity. Surprisingly, PAA electrodes tended to achieve a stable performance after the rate was reduced back to C/2, C/5, and C/10. At C/25, though, the capacity started to degrade gradually as the cycle number increased. Electrodes with PMAA, on the other hand, showed a stable recovery at C/2, and the subsequent rates showed a minimal degradation in performance. The stable cycling capacity and increased overall rate performance of electrodes with PMAA binders suggest that PMAA might be more effective in accommodating the chemical and physical changes during lithiation and delithiation, which will be discussed later.

Electrochemical impedance spectroscopy (EIS) was used to measure the internal resistance of the cells with both PAA and PMAA binders. EIS measurements were taken before electrochemical cycling, after 1 cycle (after delithiation), and after 10 cycles (after delithiation) at a C/10 rate. As shown in Figure 3b, the Nyquist plots before cycling had a high-frequency intercept attributed to the Ohmic resistance (R_{OHM}), a suppressed semi-circle in the high- to medium-frequency region attributed to the charge transfer resistance (R_{CT}), and an inclined line in the low-frequency region attributed to the Warburg impedance [35]. After cycling, as shown in Figure 3c,d, there was an additional suppressed semi-circle that is attributed to the resistance of the SEI (R_{SEI}). The equivalent circuit model used to fit the data and obtain respective resistance values is shown in Figure S4. The corresponding fitting values are shown in Table S1. Before cycling, both electrodes exhibited comparable Ohmic resistance. However, the R_{CT} of cells with a PAA binder (85.55 Ω) was higher than those with PMAA (58.11 Ω). After one cycle, the R_{ohm} of cells with a PAA binder remained the same, whilst that of PMAA increased from 5.19 Ω to 12.89 Ω. The R_{CT} of cells with a PAA binder decreased after the first cycle and then increased again after the 10th cycle. The R_{CT} of electrodes with PMAA binder increased as the cycle number increased. The relatively low R_{CT} of electrodes with PAA does not necessarily imply superior performance. R_{CT} is a measure of the reaction kinetics, which has information about the exposed area, not just the ability to transfer electrons; thus, a relatively low R_{CT} only implies

that there is lower resistance to electron flow at the electrode surface of cells with PAA binder as compared to those with a PMAA binder, which may arise from factors such as large surface cracks [36]. The large cracks may increase the electrochemically accessible surface area, leaving more sites available for charge transfer and potentially lowering the charge transfer resistance. However, the cracks may simultaneously disrupt electron pathways between the electrode materials, thereby contributing to increased electronic resistance. Thus, a lower charge transfer resistance does not imply improved electrode integrity or superior electrochemical performance.

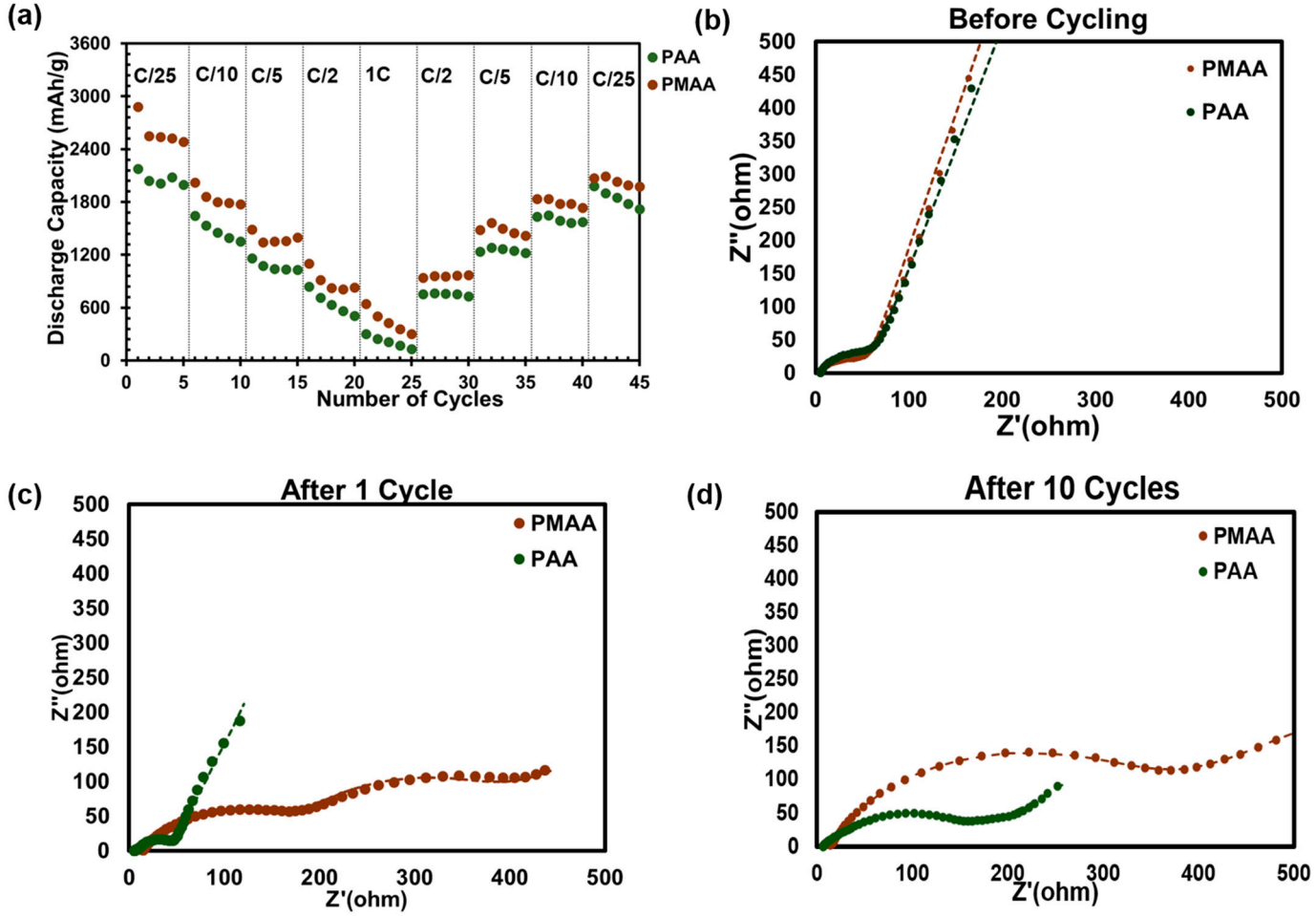

Figure 3. (**a**) Rate capability of electrodes with PMAA and PAA binders. Electrochemical impedance spectra of cells with PMAA and PAA binders: (**b**) before cycling; (**c**) after 1 cycle; and (**d**) after 10 cycles.

3.2. Morphological Changes

Figure 4 compares the change in surface morphology of electrodes with PAA and PMAA binders before cycling, after the first cycle, and after 10 cycles. The surface of the electrodes before cycling showed a smooth, continuous surface that was free of cracks. This implies that regardless of the binder chemistry, the initial slurry processing and drying process produced mechanically intact films. Electrodes after cycling showed significant structural changes characterized by the appearance of cracks on the surface of the electrode. The appearance of the cracks is a typical characteristic of silicon-based anodes due to the significant anisotropic volume expansion and contraction they undergo during lithiation and delithiation [37–39]. After the first cycle, the surface of the electrodes with a PAA binder showed a heterogeneous crack pattern. Some regions had wide, long, deep interconnected

cracks with crack lengths between 60 and 150 µm and crack widths between 5 and 10 µm, whilst other regions showed smaller, more dispersed crack regions with crack lengths ranging between 12 and 24 um and crack widths ranging between 1 and 3 µm. The heterogenous crack distribution can be due to uneven binder distribution, where binder-rich regions show smaller cracks and binder-poor regions show deep, long, wide interconnected cracks because they are unable to withstand volume expansion. These large cracks tend to disrupt electronic percolation pathways and accelerate capacity fading. In contrast, the surface of electrodes with a PMAA binder showed a more uniform, homogeneous, dense distribution of smaller cracks, with crack length ranging between 36 and 45 µm and crack width ranging between 2 and 5 µm. This is consistent with the PMAA binder being more homogeneously distributed across the electrode surface, enabling it to more evenly distribute the mechanical stress imposed by silicon's volume expansion.

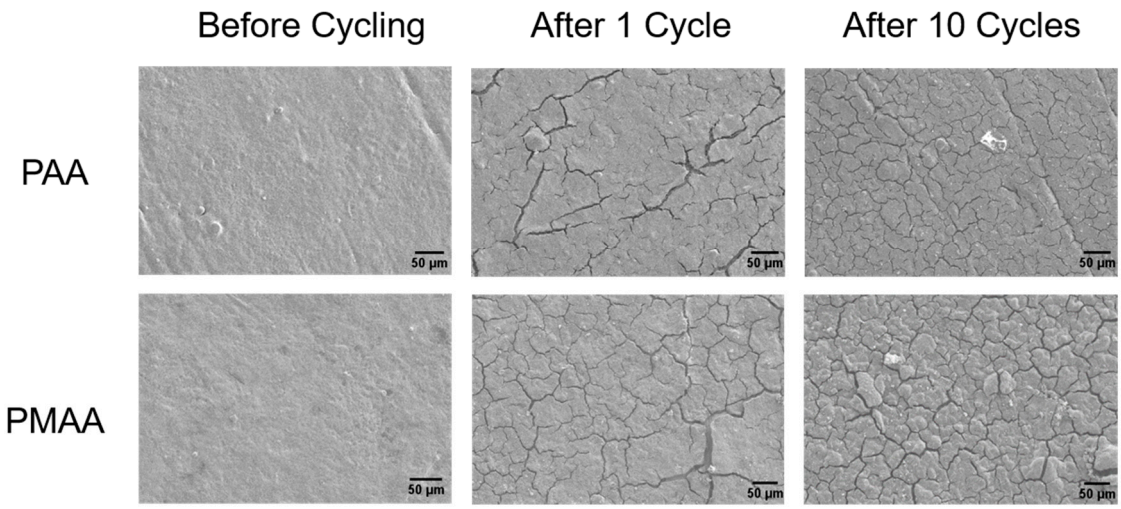

Figure 4. SEM images of silicon electrodes with PAA and PMAA binders before cycling, after 1 cycle, and after 10 cycles.

After 10 cycles, the electrodes with PAA binders showed a dense network of cracks that were relatively finer than those after the first cycle, with a crack length ranging between 32 and 80 µm. However, these cracks were numerous, leading to more isolated regions that could potentially disrupt electron pathways and also expose fresh silicon surface to further electrolyte reduction. Electrodes with PMAA still maintained a smaller, dense, evenly distributed microcrack network but with some finer cracking, with a crack length ranging between 36 and 53 µm, while still maintaining overall film continuity. The SEM results suggest that the high impedance observed in the voltage profile in Figure 2b as the cycle number increased might be due to the uneven distribution of binder on the electrodes with PAA binders, resulting in a heterogeneous microstructure after the first cycle and ultimately leading to isolated regions with poor electronic pathways and high resistance.

3.3. Structure and Chemistry of the SEI on Silicon Anodes with PAA and PMAA

Though the SEM images provided a glimpse into the structural changes at the macroscale, they do not provide sufficient resolution to provide insights into the nanoscale features of the SEI. Thus, TEM was used to visualize the structure of the SEI on the surface of the silicon anodes. To achieve this, TEM images were taken before electrochemical treatment and after 10 cyclic voltammetry (CV) cycles between 0.05 and 1.5 V. As shown in Figure 5a (PAA before cycling) and 5b (PMAA before cycling), before cycling the silicon particles had smooth edges and appeared to be spherical in shape, showing that no damage occurred prior to cycling. In Figure 5c, after cycling 10 times, the electrode with a PAA

binder showed no clear distinction between the silicon particle and the SEI. The SEI appears to have intertwined with the silicon particle, resulting in an ill-defined structure. This shows that the SEI layer on the silicon anode with a PAA binder was not able to withstand the volume expansion, leading to continuous cracks in the silicon particle, exposing fresh silicon surface to continuous electrolyte reduction and furthering SEI growth, eventually leading to an amorphous solid mixture of Si/SEI (explaining trends in the SEI, EIS, and charge/discharge above). In Figure 5d, the Si in the electrode with the PMAA binder was able to mostly maintain its structural integrity after the 10 cycles. A dense layer with varying thickness was observed around the surface of the silicon particle, indicative of a stable SEI layer. Compared to electrodes with PAA binders, the SEI on the electrodes with PMAA binders appeared to be thicker, with uneven thickness across the surface of the silicon particle. This is consistent with prior sorption studies of PAA vs. PMAA to silica nanoparticles that point to the electrostatic and solvation differences discussed above. A thick binder coating could be better able to plastically deform during Si lithiation expansion without rupturing (possibly aided by electrolyte plasticization). This might enable gradual SEI growth with PMAA rather than continuous SEI rupturing and reformation with PAA. A gradual thickening of the SEI layer reduces the lithium loss per cycle. Thus, the relatively higher and stable coulombic efficiency could be attributed to the reduced lithium-trapping and fewer SEI-forming side reactions in electrodes with PMAA binders.

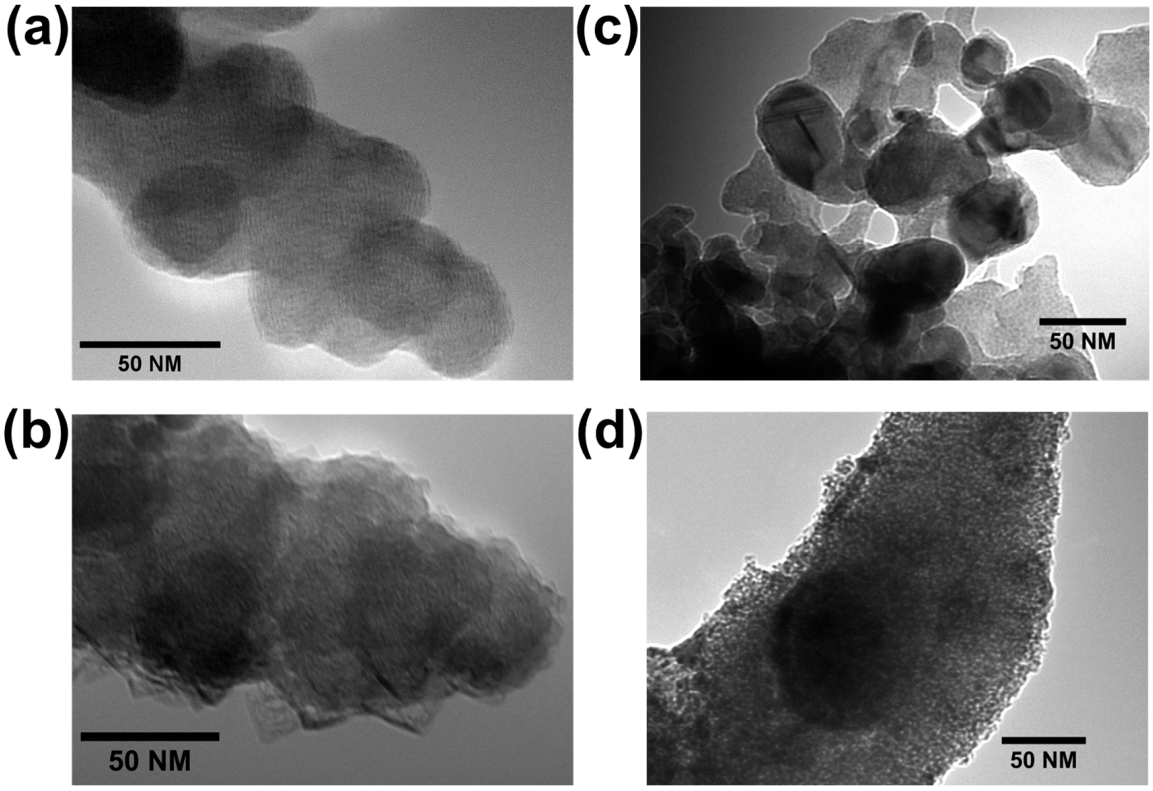

Figure 5. Transmission Electron Microscopy images of electrodes before cycling, (**a**) PAA and (**b**) PMAA, and after cycling, (**c**) PAA and (**d**) PMAA.

Next, XPS was used to analyze the chemical composition of the SEI after 1 cycle and after 10 cycles. For comparison, XPS analysis was also performed on the anodes before cycling. Figure 6a–e shows the C 1s, Li 1s, F 1s, and O 1s spectra of silicon before cycling and after charging 1 and 10 cycles at C/10. It is important to note that the chemical species identified in each (indicated by deconvoluting the C 1s, Li 1s, F 1s, and O 1s spectra) were the same for the two electrodes, which implies that the chemical species of the SEI formed

on the two electrodes were similar. However, the respective amount of each species varied across binder type and number of cycles. This suggests that the difference in electrochemical performance is not due to the presence of distinct SEI species but due to the interaction of the binder with the silicon particles, which leads to the presence of more or less of a particular SEI species.

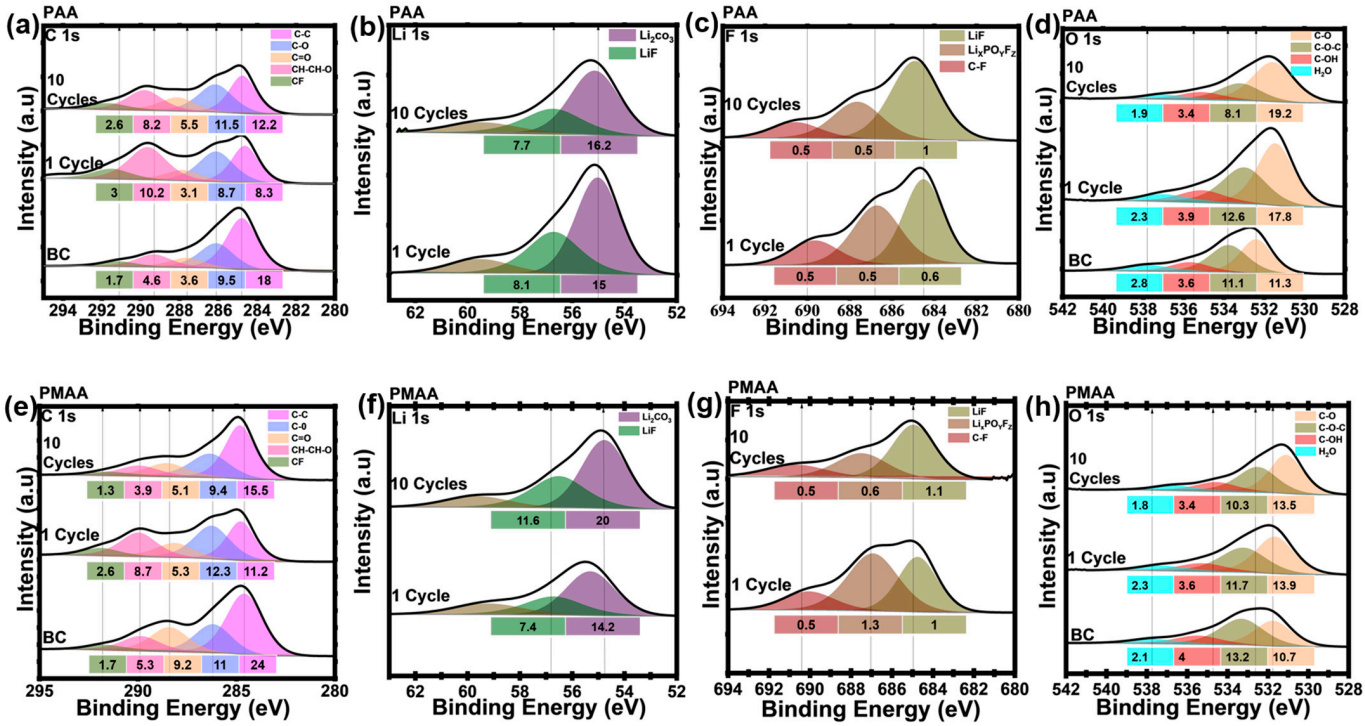

Figure 6. (**a**) C 1s; (**b**) Li 1s; (**c**) F 1s; and (**d**) O 1s XPS spectra for electrodes with PAA binder (**a**–**d**) and PMAA binder (**e**–**h**).

Figure 6a shows the C 1s spectra peaks at 284.6, 286.2, 288.4, 289.9, and 291.8 eV corresponding to the C-C, C-O, C=O, CH-CH-O, and CF, respectively [40]. The C-C peak at 284.6 eV is from Super P carbon (conducting material), and the C-O peak at 286.2 is related to hydroxyl groups in the binder. The O 1s spectra contained peaks at ~532.4, 533.3, 535.5, and 537.8 eV corresponding to C-O, C-O-C, C-OH, and H_2O species, respectively (Figure 6d) [41]. The peak at 531.7 eV (related to oxide species on the silicon surface and the binder) was a combination of SiO_x, C-O, and C=O. The peak at 533.3 eV is primarily dominated by the hydroxyl groups of the polymer. The F 1s spectra (Figure 6c,f) contained characteristic peaks at 684.8, 687.8, and 690 eV corresponding to LiF, $Li_XPO_YF_Z$, and C-F, respectively. The Li 1s spectra contained peaks at 55.3 and 56.7 eV corresponding to the Li_2CO_3 and LiF species, respectively (Figure 6 b,f). The Si 2p spectra is shown in Figure S6.

In the C 1s spectra for electrodes with PAA binder, as shown in Figure 6a, the peak at 289.9 was attributed to ether and ether carbonate species [42]. After one cycle, there was a 122% increase in the atomic percentage of these species, which confirms a reduction in the electrolyte solvents in the first cycle to form the initial SEI. After the first cycle, a new peak was observed at 531.4 eV in the O 1s spectra, which corresponds to the C-O species. These species are characteristic of polycarbonate, lithium alkyl carbonate, and lithium carbonate species—all known to contribute to the SEI, where the Li_2CO_3 species is from the decomposition of the electrolyte and the LiF species is from the decomposition of $LiPF_6$ [43]. After 10 cycles, electrodes with PAA showed a 19.2% decrease in the atomic percentage of electrolyte solvent decomposition species in the C 1s spectra, and there was no significant change in the atomic percentage of the species in the Li 1s and F 1s spectra

after 10 cycles. This suggests that the composition of the SEI does not change significantly after one cycle.

For electrodes with a PMAA binder, there was a 64% increase in the atomic percentage of electrolyte decomposition products after the first cycle, which is less than that of the PAA. This implies there is a higher degree of electrolyte decomposition in electrodes with PAA in the first cycle, agreeing with the lower first-cycle coulombic efficiency in Figure 2a. After 10 cycles, there was a significant increase in the percentages of LiF and Li_2CO_3 species, indicating that there was continuous decomposition of the $LiPF_6$ species, and that it was present in larger amounts than in the PAA electrodes. The EDS maps in Figure S7 show a high concentration of fluorinated species overlapping with Li, which confirms the abundance of inorganic LiF species in the electrodes with PMAA binder. Inorganic SEI species such as LiF and Li_2CO_3 have a Young's modulus of about 60 GPa, which is highly desirable for a mechanically robust SEI [44]. Thus, as the SEI on the electrode with PMAA binder grew, it was more intact than on PAA electrodes and mechanically robust enough to accommodate the volume expansion of the silicon anode. This mechanism is consistent with a study by Lee et al., who showed that a LiF-rich SEI protects the electrode surface against further electrolyte decomposition [45]. Also, according to Kim et al., a highly fluorinated SEI suppresses Li inventory loss [42]. The SEI formed with a PMAA binder had a higher fluorine content than the SEI formed with a PAA binder. This goes a long way to support the hypothesis that the gradual thickening of the SEI on the electrode with PMAA prevented lithium-trapping.

3.4. Degree of Phase Separation

It was suggested above that the heterogeneous crack pattern in the PAA electrodes could be due to the presence of binder-rich and binder-poor regions in the electrode. One of the main factors that affect electrode uniformity on the industrial scale is slurry phase separation. As such, one of the effective ways to evaluate the applicability of a binder for silicon anodes is its ability to form a homogeneous slurry dispersion with silicon, the conducting material, and the solvent. A simple storage test of the slurries with the different binders can give us insights into the dispersion stability of each solution. As seen in Figure 7, slurries with a PAA binder showed considerable phase separation with a sedimentation ratio of 85% after only a few hours of storage. This phase separation behavior of PAA-based slurries is widely reported in the literature [46,47], where Yim et al. showed that PAA-based slurries show 20% phase separation after storage for 7 days even after intense, commercial-like mixing [47]. This precipitation may be due to the stronger binding of PAA to Si that could induce bridging flocculation where extended aggregate networks settle from the dispersion.

In contrast, slurries with PMAA did not markedly phase separate after 3 days of storage with only moderate stirring. This stability may be associated with PMAA being less hydrophilic, leading to thicker Si particle coatings and being more weakly attracted to the Si surface to avoid bridging flocculation. The lower hydrophilicity may also improve PMAA compatibility with the conductive carbon additives. Another important consideration is the pH. The measured pH of the PAA binder slurry was 2, and that of PMAA binder slurry was 3. Prior studies have shown that PAA slurries with a pH above this can exhibit limited absorption onto SiO_2 surfaces due to repulsive electrostatics combined with PAA's high affinity towards water. In contrast, PMAA was found to exhibit high-affinity isotherms with a ~20x higher extent of saturated sorption on SiO_2 surfaces [47]. This shows that PMAA binder slurries yield better electrode uniformity compared to PAA-based slurries—again, supported by the SEM images, where electrodes with a PMAA binder after cycling show uniform crack distribution throughout the surface of the electrode whilst electrodes

with PAA binder show heterogenous crack distribution. The superior performance of the electrodes made with a PMAA binder can be attributed to the formation of a uniform electrode, leading to better stress distribution throughout the electrode.

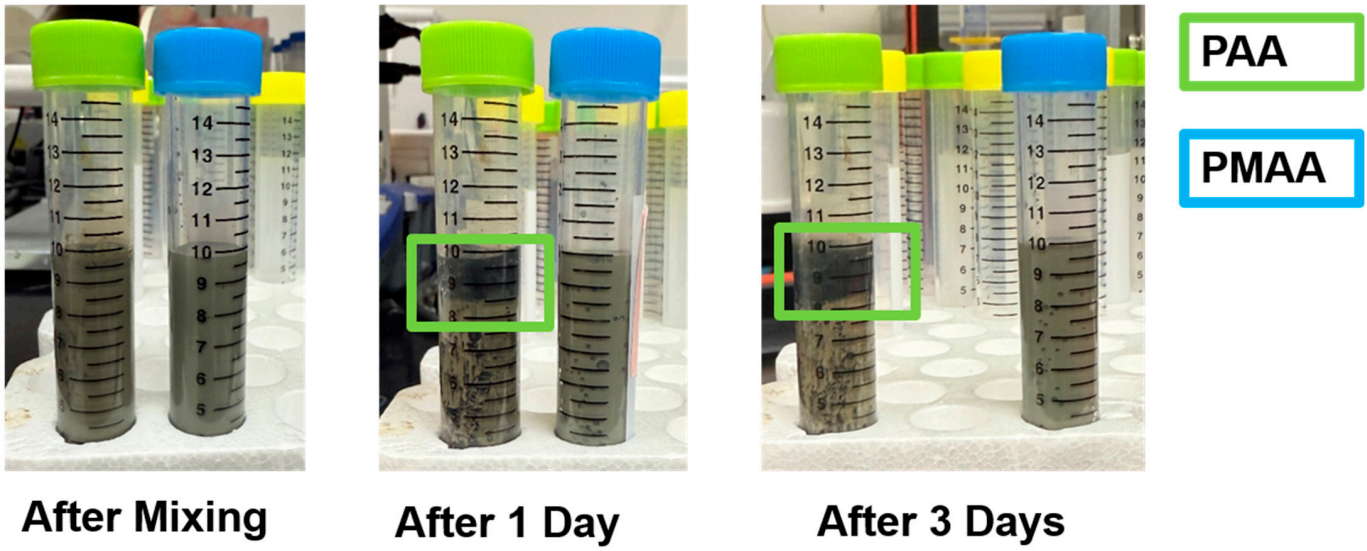

Figure 7. Degree of phase separation behavior in dilute slurries with PAA and PMAA binders.

Therefore, the PMAA binder led to achieving higher capacity when used as a Li-ion anode due to its ability to facilitate better dispersions with thicker coatings that can deform with Si during lithiation expansion. Future studies will focus on combining PMAA with more advanced Si anodes to demonstrate long-life practical batteries for future EV applications.

4. Conclusions

In summary, the effect of a PMAA binder on the structure and chemistry of the SEI on silicon-based anodes was investigated. A combination of SEM, TEM, and XPS was used to understand the changes in the morphology of the electrode and the changes in the structure and chemical composition of the SEI that were induced by repeated cycling. SEM analysis suggests that homogeneous binder distribution enabled uniform electrode fabrication, leading to uniform stress distribution in silicon anodes. TEM analysis coupled with XPS revealed that binders with similar properties lead to the formation of the same SEI species. However, the mechanism and nature of the SEI formation vary. The SEI formed with PMAA binder evolved by gradual thickening on the pre-existing SEI layer rather than reformation on the fresh silicon surface, leading to less lithium-trapping. This accounts for the stable coulombic efficiency in electrodes with PMAA binders. The different behavior for PMAA may be explained by its weaker attraction to Si and less hydrophilic character, leading to thicker Si coatings that are better able to withstand plastic deformation during lithiation expansion. Furthermore, the percentage of inorganic SEI species responsible for the formation of a robust SEI is much higher with a PMAA binder than with a PAA binder. Thus, the formation of a robust SEI capable of withstanding the volume expansion accounts for the superior electrochemical performance of electrodes with PMAA binder.

Supplementary Materials: The following supporting information can be downloaded at: https://www.mdpi.com/article/10.3390/electrochem7040038/s1. Figure S1: (a) PMAA synthesis scheme via RAFT. The resulting PMAA was characterized with (b) GPC and (c) 1H-NMR; Figure S2: (a) PAA cast film (b) PMAA cast film; Figure S3: (a) Voltage profile at Cycle 60 (b) Cycling performance of electrodes made with PAA (Mw 30000 g/mol); Figure S4: Equivalent circuit used to fit the EIS data

(a) Before Cycling (b) After Cycling; Figure S5: Electrochemical performance of silicon anode with different binders (a) PAA (b) PMAA at ~1 mg/cm^2; Figure S6: Si 2p XPS Spectra for Electrodes with PAA (a) before cycling (b) 1 cycle (c) 10 Cycles and PMAA Binder (d) Before cycling (e) 1 cycle (f) 10 Cycles; Figure S7: EDS Mapping of a representative silicon anode with PMAA binder after cycling; Table S1: EIS Fitting values for PAA and PMAA at different cycles.

Author Contributions: Conceptualization, M.S. and W.E.M.; Methodology, W.E.M.; Formal analysis, B.A.A., M.W., S.K.B. and W.E.M.; Investigation, B.A.A., M.W. and S.K.B.; Data curation, B.A.A.; Writing—original draft, B.A.A.; Writing—review and editing, B.A.A. and W.E.M.; Visualization, B.A.A.; Supervision, M.S. and W.E.M.; Project administration, W.E.M.; Funding acquisition, M.S. and W.E.M. All authors have read and agreed to the published version of the manuscript.

Funding: The authors would like to acknowledge financial support through the SC Fraunhofer USA Alliance (SCFUSA), where the overall cost of the project was split between Pomega Energy Storage Solutions and the South Carolina Department of Commerce. X-ray photoelectron Spectroscopy (XPS) data were collected at the University of South Carolina XPS Facility (RRID: SCR_026176), financially supported by the office of the Vice President for Research. M.S. and M.W. acknowledge support by the U.S. Department of Energy, Office of Science, Basic Energy Sciences, under Award No. DE-SC0023377.

Institutional Review Board Statement: Not applicable.

Informed Consent Statement: Not applicable.

Data Availability Statement: The data presented in this study are available on request from the corresponding author.

Conflicts of Interest: The authors declare that this study received partial funding from Pomega Energy Storage Solutions. The funder was not involved in the study design, collection, analysis, interpretation of data, the writing of this article or the decision to submit it for publication.

References

1. Van Fan, Y.; Perry, S.; Klemeš, J.J.; Lee, C.T. A review on air emissions assessment: Transportation. *J. Clean. Prod.* **2018**, *194*, 673–684. [CrossRef]
2. Mac Kinnon, M.; Zhu, S.; Carreras-Sospedra, M.; Soukup, J.V.; Dabdub, D.; Samuelsen, G.; Brouwer, J. Considering future regional air quality impacts of the transportation sector. *Energy Policy* **2019**, *124*, 63–80. [CrossRef]
3. Papoutsoglou, M.; Rigas, E.S.; Kapitsaki, G.M.; Angelis, L.; Wachs, J. Online labour market analytics for the green economy: The case of electric vehicles. *Technol. Forecast. Soc. Change* **2022**, *177*, 121517. [CrossRef]
4. Camargos, P.H.; dos Santos, P.H.J.; dos Santos, I.R.; Ribeiro, G.S.; Caetano, R.E. Perspectives on Li-ion battery categories for electric vehicle applications: A review of state of the art. *Int. J. Energy Res.* **2022**, *46*, 19258–19268. [CrossRef]
5. Duan, J.; Tang, X.; Dai, H.; Yang, Y.; Wu, W.; Wei, X.; Huang, Y. Building safe lithium-ion batteries for electric vehicles: A review. *Electrochem. Energy Rev.* **2020**, *3*, 1–42. [CrossRef]
6. Wu, F.; Maier, J.; Yu, Y. Guidelines and trends for next-generation rechargeable lithium and lithium-ion batteries. *Chem. Soc. Rev.* **2020**, *49*, 1569–1614. [CrossRef] [PubMed]
7. Dou, F.; Shi, L.; Chen, G.; Zhang, D. Silicon/carbon composite anode materials for lithium-ion batteries. *Electrochem. Energy Rev.* **2019**, *2*, 149–198. [CrossRef]
8. Li, J.; Klöpsch, R.; Stan, M.C.; Nowak, S.; Kunze, M.; Winter, M.; Passerini, S. Synthesis and electrochemical performance of the high voltage cathode material Li [Li0. 2Mn0. 56Ni0. 16Co0. 08] O2 with improved rate capability. *J. Power Sources* **2011**, *196*, 4821–4825.
9. Shi, J.; Xiao, D.; Ge, M.; Yu, X.; Chu, Y.; Huang, X.; Zhang, X.; Yin, Y.; Yang, X.; Guo, Y.; et al. High-capacity cathode material with high voltage for Li-ion batteries. *Adv. Mater.* **2018**, *30*, 1705575. [CrossRef] [PubMed]
10. Dasari, H.; Eisenbraun, E. Predicting capacity fade in silicon anode-based Li-ion batteries. *Energies* **2021**, *14*, 1448. [CrossRef]
11. Ozanam, F.; Rosso, M. Silicon as anode material for Li-ion batteries. *Mater. Sci. Eng. B* **2016**, *213*, 2–11. [CrossRef]
12. Feng, K.; Li, M.; Liu, W.; Kashkooli, A.G.; Xiao, X.; Cai, M.; Chen, Z. Silicon-based anodes for lithium-ion batteries: From fundamentals to practical applications. *Small* **2018**, *14*, 1702737. [CrossRef] [PubMed]
13. Li, Y.; Lv, L.; Liang, R.; Wang, L.; Wang, Y.; Qu, Q.; Shen, M.; Zheng, H. Essence of electrochemical prelithiation of the silicon anode: From the interface to the bulk phase. *J. Mater. Chem. A Mater.* **2024**, *12*, 20045–20055. [CrossRef]
14. Jia, H.; Zou, L.; Gao, P.; Cao, X.; Zhao, W.; He, Y.; Engelhard, M.H.; Burton, S.D.; Wang, H.; Ren, X.; et al. High-performance silicon anodes enabled by nonflammable localized high-concentration electrolytes. *Adv. Energy Mater.* **2019**, *9*, 1900784. [CrossRef]

15. Zheng, C.; Wu, J.; Zhang, L.; Wang, H. Vital roles of fluoroethylene carbonate in electrochemical energy storage devices: A review. *J. Mater. Chem. C Mater.* **2023**, *11*, 344–363. [CrossRef]
16. Shen, T.; Yao, Z.; Xia, X.; Wang, X.; Gu, C.; Tu, J. Rationally designed silicon nanostructures as anode material for lithium-ion batteries. *Adv. Eng. Mater.* **2018**, *20*, 1700591. [CrossRef]
17. Huang, G.; Han, J.; Lu, Z.; Wei, D.; Kashani, H.; Watanabe, K.; Chen, M. Ultrastable silicon anode by three-dimensional nanoarchitecture design. *ACS Nano* **2020**, *14*, 4374–4382. [CrossRef] [PubMed]
18. Schnabel, M.; Arca, E.; Ha, Y.; Stetson, C.; Teeter, G.; Han, S.-D.; Stradins, P. Enhanced interfacial stability of Si anodes for Li-ion batteries via surface SiO2 coating. *ACS Appl. Energy Mater.* **2020**, *3*, 8842–8849. [CrossRef]
19. Jiang, S.; Hu, B.; Shi, Z.; Chen, W.; Zhang, Z.; Zhang, L. Re-engineering poly (acrylic acid) binder toward optimized electrochemical performance for silicon lithium-ion batteries: Branching architecture leads to balanced properties of polymeric binders. *Adv. Funct. Mater.* **2020**, *30*, 1908558. [CrossRef]
20. Zhu, W.; Zhou, J.; Xiang, S.; Bian, X.; Yin, J.; Jiang, J.; Yang, L. Progress of binder structures in silicon-based anodes for advanced lithium-ion batteries: A mini review. *Front. Chem.* **2021**, *9*, 712225. [CrossRef] [PubMed]
21. Zhu, R.; Liu, S.; Li, T.; Yang, D. Precisely Prelithiated Polyacrylic Acid Binder Improving Electrochemical Performance of Micron-Sized Silicon Anodes for Lithium-Ion Batteries. *ChemElectroChem* **2024**, *11*, e202400326. [CrossRef]
22. Han, L.; Liu, T.; Sheng, O.; Liu, Y.; Wang, Y.; Nai, J.; Zhang, L.; Tao, X. Undervalued roles of binder in modulating solid electrolyte interphase formation of silicon-based anode materials. *ACS Appl. Mater. Interfaces* **2021**, *13*, 45139–45148. [CrossRef] [PubMed]
23. Eshetu, G.G.; Figgemeier, E. Confronting the challenges of next-generation silicon anode-based lithium-ion batteries: Role of designer electrolyte additives and polymeric binders. *ChemSusChem* **2019**, *12*, 2515–2539. [CrossRef] [PubMed]
24. Ramdhiny, M.N.; Jeon, J. Design of multifunctional polymeric binders in silicon anodes for lithium-ion batteries. *Carbon Energy* **2024**, *6*, e356. [CrossRef]
25. Parikh, P.; Sina, M.; Banerjee, A.; Wang, X.; D'souza, M.S.; Doux, J.-M.; Wu, E.A.; Trieu, O.Y.; Gong, Y.; Zhou, Q.; et al. Role of Polyacrylic Acid (PAA) Binder on the Solid Electrolyte Interphase in Silicon Anodes. *Chem. Mater.* **2019**, *31*, 2535–2544. [CrossRef]
26. Chen, J.; Li, Y.; Wu, X.; Min, H.; Wang, J.; Liu, X.; Yang, H. Dynamic hydrogen bond cross-linking binder with self-healing chemistry enables high-performance silicon anode in lithium-ion batteries. *J. Colloid Interface Sci.* **2024**, *657*, 893–902. [CrossRef] [PubMed]
27. Li, J.; Wu, Z.; Lu, Y.; Zhou, Y.; Huang, Q.; Huang, L.; Sun, S. Water soluble binder, an electrochemical performance booster for electrode materials with high energy density. *Adv. Energy Mater.* **2017**, *7*, 1701185. [CrossRef]
28. Miranda, A.; Sarang, K.; Gendensuren, B.; Oh, E.-S.; Lutkenhaus, J.; Verduzco, R. Molecular design principles for polymeric binders in silicon anodes. *Mol. Syst. Des. Eng.* **2020**, *5*, 709–724. [CrossRef]
29. Bhat, A.L.; Shaju, A.; Su, Y.-S. Binder engineering for prelithiated SiOx anodes in lithium-ion batteries. *J. Energy Storage* **2026**, *169*, 122726. [CrossRef]
30. Song, M.; Hwang, J.; Son, J.; Park, M.; Kim, G.; Lim, N.; Woo, S.; Lee, T.K.; Song, S.; Song, W. A Study on Polymer Binders for High-Capacity Silicon Anode: Effect of Prelithiation Precursors. *Small Struct.* **2025**, *6*, e202500423. [CrossRef]
31. Hu, B.; Jiang, S.; Shkrob, I.A.; Zhang, J.; Trask, S.E.; Polzin, B.J.; Jansen, A.; Chen, W.; Liao, C.; Zhang, Z.; et al. Understanding of pre-lithiation of poly(acrylic acid) binder: Striking the balances between the cycling performance and slurry stability for silicon-graphite composite electrodes in Li-ion batteries. *J. Power Sources* **2019**, *416*, 125–131. [CrossRef]
32. Fairley, N.; Fernandez, V.; Richard-Plouet, M.; Guillot-Deudon, C.; Walton, J.; Smith, E.; Flahaut, D.; Greiner, M.; Biesinger, M.; Tougaard, S.; et al. Systematic and collaborative approach to problem solving using X-ray photoelectron spectroscopy. *Appl. Surf. Sci. Adv.* **2021**, *5*, 100112. [CrossRef]
33. Gaur, U.; Lau, S.; Wunderlich, B.B.; Wunderlich, B. Heat capacity and other thermodynamic properties of linear macromolecules VI. Acrylic polymers. *J. Phys. Chem. Ref. Data* **1982**, *11*, 1065–1089. [CrossRef]
34. Guo, M.-J.; Xiang, C.-C.; Hu, Y.-Y.; Deng, L.; Pan, S.-Y.; Lv, C.; Chen, S.-X.; Deng, H.-T.; Sun, C.-D.; Li, J.-T.; et al. A dual force cross-linked γ-PGA-PAA binder enhancing the cycle stability of silicon-based anodes for lithium-ion batteries. *Electrochim. Acta* **2022**, *425*, 140704. [CrossRef]
35. Teliz, E.; Zinola, C.F.; Díaz, V. Identification and quantification of ageing mechanisms in Li-ion batteries by Electrochemical impedance spectroscopy. *Electrochim. Acta* **2022**, *426*, 140801. [CrossRef]
36. Raulo, A.; Lateef, S.A.; Jalilvand, G. An Expansion-Mitigant Binder for Stable Cycling of High-Loading Lithium–Sulfur Batteries. *ACS Appl. Mater. Interfaces* **2025**, *17*, 26604–26619. [CrossRef] [PubMed]
37. Li, J.-Y.; Xu, Q.; Li, G.; Yin, Y.-X.; Wan, L.-J.; Guo, Y.-G. Research progress regarding Si-based anode materials towards practical application in high energy density Li-ion batteries. *Mater. Chem. Front.* **2017**, *1*, 1691–1708. [CrossRef]
38. Pervez, A.; Choi, T.; Lee, D.; Mun, Y.; Oh, P.; Cha, J.; Son, Y. Advanced Analysis Techniques for Elucidating Failure Mechanisms in Silicon Anodes for Li-Ion Batteries. *Small* **2026**, *22*, e12223. [CrossRef] [PubMed]
39. Pervez, A.; Choi, T.; Lee, D.; Mun, Y.; Oh, P.; Cha, J.; Son, Y. Anisotropic expansion and size-dependent fracture of silicon nanotubes during lithiation. *J. Mater. Chem. A Mater.* **2019**, *7*, 15113–15122. [CrossRef]

40. He, J.; Das, C.; Yang, F.; Maibach, J. Crosslinked poly(acrylic acid) enhances adhesion and electrochemical performance of Si anodes in Li-ion batteries. *Electrochim. Acta* **2022**, *411*, 140038. [CrossRef]
41. Eshetu, G.G.; Diemant, T.; Grugeon, S.; Behm, R.J.; Laruelle, S.; Armand, M.; Passerini, S. In-Depth Interfacial Chemistry and Reactivity Focused Investigation of Lithium–Imide- and Lithium–Imidazole-Based Electrolytes. *ACS Appl. Mater. Interfaces* **2016**, *8*, 16087–16100. [CrossRef] [PubMed]
42. Kim, M.; Harvey, S.P.; Huey, Z.; Han, S.-D.; Jiang, C.-S.; Son, S.-B.; Yang, Z.; Bloom, I. A new mechanism of stabilizing SEI of Si anode driven by crosstalk behavior and its potential for developing high performance Si-based batteries. *Energy Storage Mater.* **2023**, *55*, 436–444. [CrossRef]
43. An, S.J.; Li, J.; Daniel, C.; Mohanty, D.; Nagpure, S.; Wood, D.L. The state of understanding of the lithium-ion-battery graphite solid electrolyte interphase (SEI) and its relationship to formation cycling. *Carbon* **2016**, *105*, 52–76. [CrossRef]
44. Robin, C.; Lorthioir, C.; Erman, A.; Perez, J.; Fall, A.; Ovarlez, G.; Amiel, C.; Le Cœur, C. Adsorption of poly(methacrylic acid) onto differently charged silica nanoparticles and its consequences on particles clustering. *Colloids Surf. A Physicochem. Eng. Asp.* **2022**, *638*, 128287. [CrossRef]
45. Lee, D.; Lee, S.; Jung, D.S.; Roh, K.C.; Seo, J.; Kim, J.; Kim, K.; Kim, P.J.; Choi, J. Synergistically enhanced LiF–rich protective layer for highly stable silicon anodes. *Appl. Surf. Sci.* **2024**, *661*, 160023. [CrossRef]
46. Burdette-Trofimov, M.K.; Armstrong, B.L.; Rogers, A.M.; Heroux, L.; Doucet, M.; Yang, G.; Phillip, N.D.; Kidder, M.K.; Veith, G.M. Understanding Binder–Silicon Interactions during Slurry Processing. *J. Phys. Chem. C* **2020**, *124*, 13479–13494. [CrossRef]
47. Yim, T.; Choi, S.J.; Jo, Y.N.; Kim, T.-H.; Kim, K.J.; Jeong, G.; Kim, Y.-J. Effect of binder properties on electrochemical performance for silicon-graphite anode: Method and application of binder screening. *Electrochim. Acta* **2014**, *136*, 112–120. [CrossRef]

Disclaimer/Publisher's Note: The statements, opinions and data contained in all publications are solely those of the individual author(s) and contributor(s) and not of MDPI and/or the editor(s). MDPI and/or the editor(s) disclaim responsibility for any injury to people or property resulting from any ideas, methods, instructions or products referred to in the content.